Title

Intercalation and Conversion Reactions of Nanosized β-MnO2 Cathode in the Secondary Zn/MnO2 Alkaline Battery

Journal

The Journal of Physical Chemistry C, 122(21)

ISSN

1932-7447

Authors

Seo, Joon Kyo
Shin, JaeWook
Chung, Hyeseung
et al.

Publication Date

2018-05-31

DOI

10.1021/acs.jpcc.7b11685

Peer reviewed

THE JOURNAL OF PHYSICAL CHEMISTRY C

Subscriber access provided by UNIV OF CALIFORNIA SAN DIEGO LIBRARIES

C: Energy Conversion and Storage; Energy and Charge Transport

Intercalation and Conversion Reactions of Nanosized #-MnO Cathode in the Secondary Zn/MnO Alkaline Battery

Joon Kyo Seo, JaeWook Shin, Hyeseung Chung, Po Yu Meng, Xuefeng Wang, and Ying Shirley Meng

J. Phys. Chem. C, **Just Accepted Manuscript** • DOI: 10.1021/acs.jpcc.7b11685 • Publication Date (Web): 03 May 2018

Intercalation and Conversion Reactions of Nanosized β-MnO_2 Cathode in the Secondary Zn/MnO_2 Alkaline Battery

Joon Kyo Seo,[†,‡] JaeWook Shin,[‡,§] Hyeseung Chung,[‡] Po Yu Meng,[‡] Xuefeng Wang,[‡] and Y. Shirley Meng[,†,‡]*

[†]Materials Science and Engineering, University of California San Diego, La Jolla, CA 92093, USA

[‡]Department of NanoEngineering, University of California San Diego, La Jolla, CA 92093, USA

[*]E-mail: shmeng@ucsd.edu. Tel: +1 (858) 822-4247.

[§]Present address: Advanced Battery Center, KAIST Institute for NanoCentury, Korea Advanced Institute of Science and Technology (KAIST), 291 Daehak-ro, Yuseong-gu, Daejeon, 34141, Republic of Korea

ABSTRACT

This work reports rechargeable Zn/β-MnO_2 alkaline batteries as promising stationary energy storage. Unlike commercial alkaline batteries with poor cyclic performance, the nanosized β-MnO_2 cathode in the mixture of LiOH and KOH electrolyte enables rechargeable reactions with high capacity. To unveil the underlying reaction mechanisms of nanosized β-MnO_2, we combine thermodynamic frameworks with experimental characterization including electrochemistry, X-ray diffraction, and X-ray photoelectron spectroscopy. The results demonstrate a series of proton intercalation reaction (β-MnO_2 → γ-MnOOH) and two-phase conversion reactions (γ-MnOOH → $Mn(OH)_2$ → λ-MnO_2) during the first cycle, and Li and H co-intercalation in the host structure of λ-MnO_2 spinel during the hundredth cycle. It is remarkable that the addition of Bi_2O_3 in the nanosized β-MnO_2 cathode exhibits the outstanding capacity. After one hundred discharging, the battery demonstrates a capacity of 316 mAh g^{-1}. Our findings can serve in the tailored cathode design in high capacity and rechargeable Zn/β-MnO_2 alkaline batteries.

INTRODUCTION

Ever since Lewis Urry invented a primary Zn/MnO_2 alkaline battery back in the late 1950's, it has been widely adopted as an energy source for low-power electronics. Recently, the Zn/MnO_2 aqueous battery is gaining attention as a rechargeable energy storage for smart grid technology.[1-3] Compared to a Li-ion battery, a Zn/MnO_2 aqueous battery has several advantages such as low material cost, better safety, and non-toxicity. To illustrate, the current rechargeable Zn/MnO_2 aqueous battery technology costs under \$90 per kWh,[2] whereas the cost for Li-ion batteries are unlikely to fall below \$200 per kWh.[3] In addition, Zn/MnO_2 aqueous battery operates with water-based electrolytes, furnishing a higher degree of safety making them an attractive option for grid-scale usage in residential homes and dense urban areas.

MnO_2 exists in multiple crystallographic structures including α-, β-, γ-, δ-, λ-, and R-MnO_2. These MnO_2 polymorphs are defined by different connection of the basic structural unit, MnO_6 octahedron, and various types of tunnels within the crystal structure.[4-5] Electrochemical reactions vary in Zn/MnO_2 aqueous batteries dependent on the phase of MnO_2 and electrolyte used, however, the most common discharge mechanism of MnO_2 involves a homogeneous reaction and followed by a heterogeneous reaction.[6-8] Once the discharge initiates, protons intercalate into tunnels of MnO_2 through the homogeneous reaction without Mn-O bond breakage, however the bonds begin to break in the heterogeneous reaction as the discharge proceeds further leading to eventual deformation of the lattice. During the homogeneous reaction, the voltage changes rapidly, however the heterogeneous reaction manifests the voltage plateaus due to two-phase reactions.

Recently, many studies have reported the development of rechargeable Zn/MnO_2 aqueous batteries which utilize mild acidic electrolytes.[9-11] Lee et al. describe that a Zn/α-MnO_2 system in $ZnSO_4$ electrolyte involves Zn/Zn^{2+} redox at the anode and α-MnO_2/Mn^{2+} at the cathode. An additional reversible phase of $Zn_4(OH)_6(SO_4)\cdot 5H_2O$ (zinc hydroxide sulfate) precipitates on the cathode's surface due to Zn^{2+} and SO_4^{2+} in an aqueous electrolyte.[10] Pan et al. report that the rechargeability of Zn/α-MnO_2 aqueous battery is significantly improved by adding $MnSO_4$ salt in the $ZnSO_4$ electrolyte.[11] They describe the same redox reactions proposed by Lee et al. with an undefined hydration number for the zinc hydroxide sulfate. However, the addition of the $MnSO_4$ salt in the electrolyte suppresses the dissolution of Mn^{2+} and enables longevity of over 5000 cycles.

In addition to the acidic solutions, the basic solutions have been investigated to understand the rechargeability of Zn/MnO_2 aqueous batteries. Gallaway et al. probed the phase transformation of the cathode/anode in a commercial alkaline 'AA' cell.[12] They observed $ZnMn_2O_4$ (hetaerolite) forming in the cathode, implying that it is a side product of the chemical reaction between MnOOH and $Zn(OH)_4^{2-}$. The $Zn(OH)_4^{2-}$ (zincate ion) is generated from $Zn(OH)_4^{2-}/Zn$ redox at the Zn anode which then migrates to the cathode where MnOOH is formed after MnO_2 is reduced. The $ZnMn_2O_4$ phase produced is electrochemically inactive phase and degrades the cycle performance of Zn/MnO_2 aqueous batteries. Turney et al. reported that the formation of $Zn(OH)_4^{2-}$ is favorable at the Zn anode where OH^- species are concentrated inducing the production of $ZnMn_2O_4$.[3] In another study, Hertzberg et al. found that the combination of LiOH and KOH as electrolytes in a Bi species incorporated Zn/β-MnO_2 alkaline battery improved the rechargeability demonstrating a reversible single-electron reaction for 60 cycles.[13] They proposed that a reversible reaction occurs during the cycling between the reduced phases

($Mn(OH)_2$ and $LiMn_2O_4$) and the oxidized phase (δ-MnO_2). This reaction mechanism, however, is contentious due to δ-MnO_2 being measured solely during the first charged state and not in any of the subsequent cycles.

Optimizing the utilization of two electrons in MnO_2 is an essential for high-energy stationary storage. Many studies have demonstrated that the capacity increases using nanostructured materials.[5, 14-15] Chen et al. reported that nanosized γ-MnO_2 shows almost two-times higher discharge capacity than bulk γ-MnO_2.[14] They suggested that broad surface area in nano-scale MnO_2 enlarges contact between MnO_2 active materials and an electrolyte which lowers internal resistance and facilitates proton diffusion. In order to utilize large capacity and improve the reversibility of reactions in alkaline solutions, we synthesized nanoscale β-MnO_2 and assembled the Zn/β-MnO_2 alkaline battery with the LiOH and KOH electrolytes. The discharge capacity shows 225 mAh g^{-1} at the hundredth cycle, which is higher than the capacity of the battery made of commercial β-MnO_2 by 113 mAh g^{-1}. Furthermore, we studied the phase transformation of nanosized β-MnO_2 in Zn/β-MnO_2 alkaline battery. The result indicates that the proton intercalation reaction is followed by two-phase conversion reactions at the first cycle, however, a different reaction mechanism is observed at the hundredth cycle. Li and H co-inserted λ-MnO_2 spinel and λ-MnO_2 spinel are formed at the hundredth discharged and charged state, respectively. Lastly, we incorporated β-MnO_2 cathode with 4% mole fraction of Bi_2O_3 to enhance the electrochemical performance. The discharge capacity is 316 mAh g^{-1} at the hundredth cycle. Bi-$_2O_3$ additive reacts with $Zn(OH)_4^{2-}$, which alleviates the capacity loss driven by the formation of irreversible $ZnMn_2O_4$.

EXPERIMENTAL METHODS

β-MnO_2 synthesis. β-MnO_2 was synthesized by the multiple heating steps in order to confirm Mn^{4+}, to remove NOx gases completely and crystalize nanosized β-MnO_2. The thermal decomposition process begins with dissolving 10 g of $Mn(NO_3)_2 \cdot 4H_2O$ in 16 mL deionized (D.I.) water. The solution was stirred with a magnetic bar in a round-bottom flask while being heated in the silicon-oil bath to increase the reaction temperature to 140 °C. Once the temperature reached 140 °C, the reaction was held at that temperature until the initially clear solution developed a black color with high viscosity indicating the oxidation to the Mn^{4+} state. Then, the round flask was transferred to a preheated vacuum oven and kept at 125 °C overnight to facilitate complete drying of the MnO_2 product and to eliminate excess NO_x gases. The sample was removed from the vacuum oven after 12 h and transferred to a preheated box furnace heated to 125 °C. The temperature of the oven was programmed to increase up to 325 °C with a step of 5 °C/min, then to hold the temperature at 325 °C for 5 h to crystalize nanosized β-MnO_2. After natural cooling, the solid sample was ground with a mortar and a pestle to turn it into fine powder.

Electrochemical characterization. The working electrode is composed of the β-MnO_2 active material (synthesized β-MnO_2, commercial β-MnO_2, or synthesized β-MnO_2 with 4 % mole fraction of Bi_2O_3), carbon black Super-P, and polytetrafluoroethylene (PTFE) with a 60:30:10

weight ratio. The typical mass loading of β-MnO_2 is 11.4 mg cm^{-2}. The electrode was implanted onto a Ni foam current collector and pressed using a hydraulic press with a pressure of eight tons. The pressed electrode was then covered with one layer of polyvinylidene chloride, two layers of nonwoven separator (FS 22145 from Freudenberg LLC) and a Zn plate counter electrode. They were sandwiched between two acrylic plates, which were held together tightly with screws. After an assembly, the battery was immersed in a 20 mL beaker with 10.5 mL of 1 M KOH and 3 M LiOH electrolyte. This molar ratio of 1 : 3 = KOH : LiOH was optimized for alkaline batteries in previous report.[13] Parafilm was used to seal the beaker. All batteries in this study were tested at C/10 current rate for the first cycle and C/5 for the following cycles. Considering the rate capability tests for synthesized β-MnO_2 with/without Bi_2O_3, the discharge/charge process was carried out over the course 20 cycles for each stage except for the last stage (9 cycles). Constant current rates were calculated using the theoretical two-electron capacity of MnO_2 which is 616 mAh g^{-1}. The voltage range used is $0.50 < V < 1.80$. The constant voltage of 1.80 V was applied at the end of constant current charging until the current decreased to 10% of the current rate. The batteries were cycled using an Arbin battery cycler at room temperature. In addition, the electrochemical stability window of electrolyte was measured using a Solartron 1260 Impedance Analyzer. The linear sweep voltammetry was taken on Ni foam electrodes compared against Hg/HgO reference electrode in 1M KOH and 3M LiOH electrolyte at a scan rate of 1 mV/s.

In house X-ray diffraction (XRD). The in-house XRD samples were synthesized and commercial β-MnO_2 powder, and cycled β-MnO_2 electrodes. Cycled electrodes were collected at 1.25 V, 1.05 V, 0.50 V and 1.80 V during the first cycle of synthesized β-MnO_2 in Zn/β-MnO_2 alkaline batteries. The collected electrodes were washed with running D.I. water and soaked in

the D.I. water overnight. After washing, the electrodes were dried in 60 □ for 3 hours in the oven. All the XRD data were collected at an ambient temperature on a Bruker D8 Advance diffractometer at 40 kV, 40 mA for Cu Kα (λ = 1.5418 Å), with a scan speed of 5 s per step, a step size of 0.02° in 2θ, and a 2θ range of 10–80°.

Synchrotron X-ray diffraction (SXRD). Cycled electrodes of synthesized β-MnO_2 collected at the hundredth discharge/charged state were selected for SXRD analysis. The cycled electrodes were washed with running D.I. water and soaked in the D.I. water overnight. After washing, electrodes were dried at 60 □ for 3 hours in the oven. SXRD spectra were acquired at the Advanced Photon Source (APS) at Argonne National Laboratory (ANL) on beamline 11-BM (λ= 0.4145 Å). The beamline uses a sagittal focused X-ray beam with a high precision diffractometer circle and perfect Si(111) crystal analyzer detection for high sensitivity and resolution. SXRD spectra were plotted based on λ= 1.5418 Å to compare with the in-house XRD spectra.

X-ray photoelectron spectroscopy (XPS). XPS was performed using a Kratos AXIS Supra at the Laboratory for Electron and X-ray Instrumentation. Cycled samples were prepared by washing with running D.I. water and soaking the electrode in the D.I. water overnight, and drying in 60 □ for 3 h in the oven. The XPS was operated using an Al anode source running at 15 kV. All XPS measurements were collected using a 300 μm by 700 μm spot size without using a charge neutralizer during acquisition. A step size of 0.3eV was used for survey scan and 0.1 eV was for high-resolution scans. All the spectra were calibrated with carbon 1s sp^3 at 284.8 eV.

Scanning electron microscope (SEM) and energy dispersive X-ray spectroscopy (EDS). The SEM/EDS samples selected were synthesized and commercial β-MnO_2 powders, Bi_2O_3 and immersed Bi_2O_3 powder in 6M Zn nitrate solution. The sample of immersed Bi_2O_3 powder was prepared by washing with running D.I. water, soaking the powder in the D.I. water overnight,

and drying in 60 □ for 3 h in the oven. All powder samples were loaded onto a SEM holder using a carbon adhesive tape. The images were obtained using a 15 kV energy source using the FEI/Phillips XL30 ESEM.

Computational details. First principles calculations were conducted based on spin-polarized GGA+*U* [16-17] using the Perdew–Burke–Ernzerhof of exchange and correlation functionals.[18] A plane-wave basis set and the projector-augmented wave (PAW) method [19-20] were used as parameterized in the Vienna *ab initio* simulation package (VASP).[21] A gamma point mesh is performed with 7 × 7 × 7 *k*-points for λ-MnO_2. All the atoms were fully relaxed to calculate the optimized structure with a cutoff energy of 1.3 times the maximum cutoff specified by the pseudopotentials on a plane-wave basis set. The scheme proposed by Persson et al[22] was adopted in order to obtain an accurate standard Gibbs free energy of formation.

RESULTS AND DISCUSSION

The influence of a particle size. The powder of synthesized and commercial β-MnO_2 are measured by in-house X-ray diffractometer as shown in figure 1(a). The peak broadenings are observed in synthesized β-MnO_2, however, the peak positions match the reference β-MnO_2. The XPS result confirms Mn 3s multiplet splitting with $\Delta E = 4.62$ eV in figure 1(b); this value agrees well with $\Delta E = 4.65$ eV found in commercial β-MnO_2 (Alfa Aesar) as shown in figure S1.[23] The SEM image shows agglomerated secondary particles from the synthesized β-MnO_2 (the red color box) and chunky particles with small parasites from the commercial β-MnO_2 (the orange color box) in figure 1(c). In the synthesized β-MnO_2 the primary particle is in a size range of less than 50 nm. The Brunauer–Emmett–Teller (BET) surface analysis conducted with the nitrogen sorption isotherms at -196 °C by Autosorb - iQ (Quantachrome) indicates ~21 times larger

surface area for the synthesized β-MnO_2 than the commercial β-MnO_2 in (figure S2). The cyclic performance of Zn/β-MnO_2 alkaline batteries is tested in 1 M KOH and 3 M LiOH containing electrolyte as shown in figure 1(d). The first discharge capacity of synthesized β-MnO_2 is 574 mAh g^{-1} (approximately 93% of the MnO_2's theoretical capacity of 616 mAh g^{-1}). The commercial β-MnO_2 produces 464 mAh g^{-1} during the first discharge (approximately 75% of the theoretical capacity). The discharge capacity of synthesized β-MnO_2 at the hundredth cycle is 225 mAh g^{-1}, which is higher than that of commercial β-MnO_2, 112 mAh g^{-1}. The coulombic efficiency (CE) defined by the percentage of charge capacity over discharge capacity is less than 100 %. This is due to the different amount of additional capacity produced by H_2 and O_2 gases, which are generated within the battery's operating voltage (figure S3). The gases are released from the customized beaker cell and its configuration is demonstrated in the experimental. Another factor affecting the CE is the size of β-MnO_2. We estimate that bulk β-MnO_2 materials, which have relatively small surface-area-to-volume ratio do not promote the formation of irreversible $ZnMn_2O_4$ phase, resulting in relatively higher CE than the synthesized β-MnO_2 nanomaterials. In case of synthesized β-MnO_2 nanomaterials, it improves the specific capacity during cycles, however it promotes the formation of $ZnMn_2O_4$ phase at the same time due to its large surface-area-to-volume ratio.

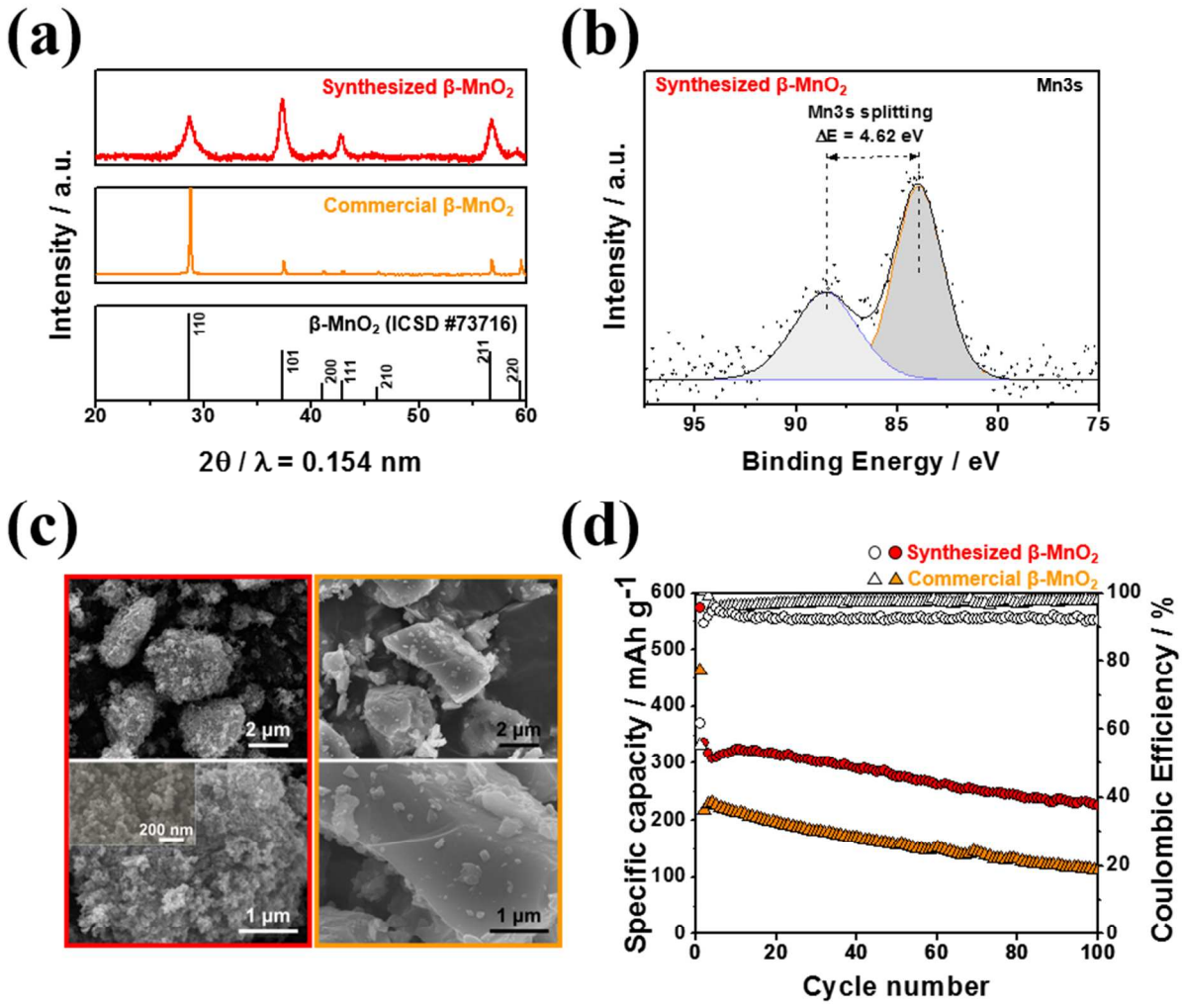

Figure 1. (a) In-house XRD patterns for synthesized and commercial β-MnO_2 (Alfa Aesar); (b) Mn 3s splitting in the XPS result of synthesized β-MnO_2; (c) SEM images for synthesized (red box) and commercial β-MnO_2 (orange box); (d) Cyclic performance for synthesized β-MnO_2 and commercial β-MnO_2 at C/10 current rate for the first cycle and C/5 for the following cycles.

The gap between the discharge capacities from two batteries is most likely due to the difference between particle sizes of the active materials. The nanoscale β-MnO_2 particles have broader electrochemical surface area than the bulk β-MnO_2 particles, which increases the effective contact points with the electrolyte, lowering internal resistance and shortening diffusion

pathways.[5, 15] In addition, insufficiently coordinated surface atoms of the synthesized β-MnO_2 nanoparticles are expected to facilitate chemical adsorptions from aqueous solutions and undergo electrochemical reactions. Han et al. reported the effect of the nanosized particle on an adsorption energy of chemicals in aqueous media.[24] It shows that the adsorption energy of chemicals on the surface of a nanoparticle is stronger than that on the surface of a bulk material. Nanoparticles hold a high ratio of undercoordinated surface atoms to coordinated atoms, thus their chemisorption is greater than that of the bulk materials. The nanosized β-MnO_2 case are expected to undergo facile electrochemical reactions once H_2O adsorption from aqueous electrolytes has occurred. The reaction mechanism of synthesized β-MnO_2 will be discussed further in this study. Another factor to consider regarding surface chemisorption is the cohesive energy per atom of a nanoparticle.[25] Constituent atoms in a nanoparticle are bound together with weak cohesive energy, which is a less stable formation than a bulk material. Thus nanoparticles in aqueous media are likely to bind with nearby molecules for stabilization, which in turn stimulates electrochemical reactions.

The reaction mechanism of nanosized β-MnO_2 during the first cycle. *Ex situ* in-house XRD patterns are measured for synthesized β-MnO_2 cathodes during the first cycle of Zn/β-MnO_2 alkaline batteries (figure 2). The reaction mechanism of synthesized β-MnO_2 nanomaterial is proposed as follows:

Electrochemical reaction (the first discharge):

$$\beta\text{-}MnO_2 + H_2O + e^- \rightarrow \gamma\text{-}MnOOH + OH^- \quad (1)$$

$$\gamma\text{-}MnOOH + H_2O + e^- \rightarrow Mn(OH)_2 + OH^- \quad (2)$$

Electrochemical reaction (the first charge):

$$Mn(OH)_2 + 2OH^- \rightarrow \lambda\text{-}MnO_2 + 2H_2O + 2e^- \quad (3)$$

$$1/3Mn_3O_4 + 4/3OH^- \rightarrow \lambda\text{-}MnO_2 + 2/3H_2O + 4/3e^- \quad (4)$$

Chemical reaction:

$$\gamma\text{-}MnOOH + 1/2Mn(OH)_2 \rightarrow 1/2Mn_3O_4 + H_2O \quad (5)$$

To further validate the reaction mechanism characterized by *ex situ* in-house XRD patterns, the theoretical reaction voltage (E) for each electrochemical reaction proposed in Eq. (1-4) is calculated by applying the Nernst equation as follows:

$$E = E° + 2.303 \square RT/F \square pOH - (-1.119)\ V\ vs.\ Zn(OH)_4^{2-} | Zn \quad (6)$$

where E° is the standard reduction potential (table S1) which is obtained by the standard Gibbs free energy of formation (table S2); R is the gas constant (8.314 J K^{-1} mol^{-1}); T is the room temperature (298.15 K); F is the Faraday constant (96485 C mol^{-1}); pOH is the concentration of hydroxide. The theoretical value of pOH = -0.6 (pH = 14.6) is used since the electrolyte consists of 1 M KOH and 3 M LiOH, where 4 M OH^- exists in total. In alkaline media, the Zn anode has a redox couple with $Zn(OH)_4^{2-}$.[12, 26] The theoretical reaction voltage is therefore measured with respect to the standard reduction potential of $Zn(OH)_4^{2-}$ | Zn (1.119 V vs. SHE).[27] The ideal voltage curve of a Zn/β-MnO_2 alkaline battery fabricated with synthesized β-MnO_2 nanomaterial is presented in figure 2(b). The theoretical voltage profile (dotted line) matches well with the experimental voltage profile, which will be discussed in detail.

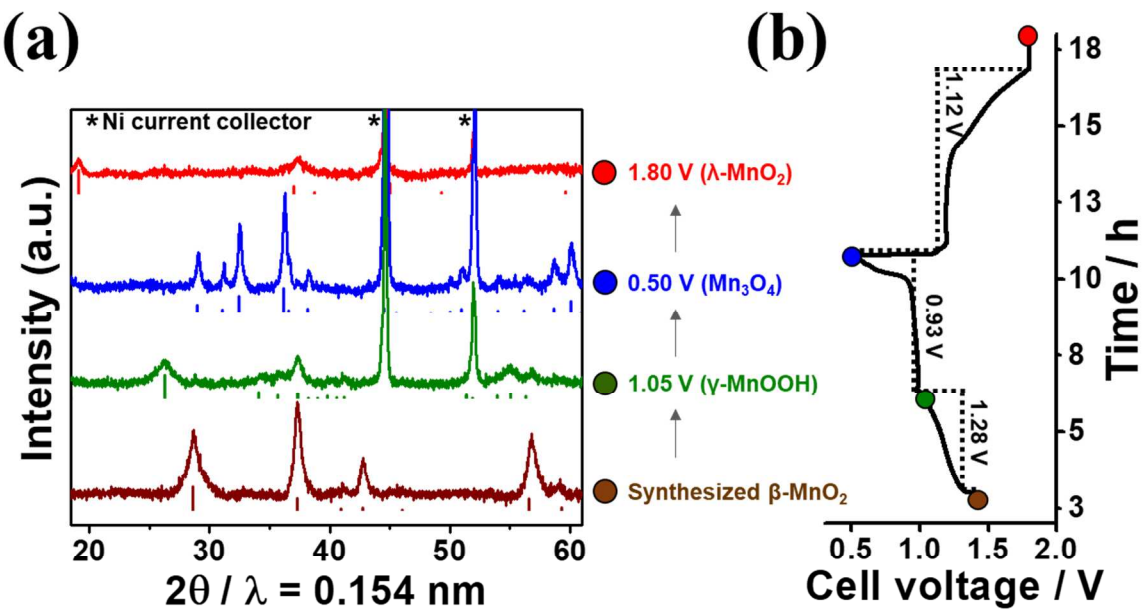

Figure 2. (a) *Ex situ* in-house XRD patterns for synthesized β-MnO_2 nanomaterial and its intermediate phases during the first cycle. The vertical line presents XRD patterns from ICSD database (β-MnO_2: #73716, γ-MnOOH: #84949, Mn_3O_4: #643199, and λ-MnO_2: #193445). Detailed XRD patterns are shown in figure S4. (b) The voltage profile for the first discharge/charge of a Zn/β-MnO_2 alkaline battery at C/10 current rate. The colored circles represent points that synthesized β-MnO_2 nanomaterial and cycled β-MnO_2 cathode samples are collected. The dotted line indicates the theoretical voltage profile at pH=14.6.

As mentioned above, XRD analysis shown in figure 2(a) indicates that the synthesized powder is β-MnO_2. β-MnO_2 has a tetragonal crystal lattice where Mn-O octahedrons are connected in a corner-sharing and an edge-sharing configurations as shown in figure 3. Void tunnels and Mn-O octahedrons are positioned 1 x 1. Upon the initiation of the first discharge, protons originating from H_2O molecules adsorbed on the surface of nanosized β-MnO_2 intercalate into the void tunnels and form γ-MnOOH at the end of the first-electron reaction (Eq. (1)). The XRD pattern

of γ-MnOOH is obtained during the first discharge at 1.05 V (figure 2). γ-MnOOH is a monoclinic crystal lattice where the original 1 x 1 void tunnels in β-MnO_2 are occupied with protons, resulting in a distortion in the lattice (figure 3). The XRD spectrum acquired at 1.25 V during the early stage of proton intercalation at the first discharge shows the overall peak intensity of β-MnO_2 decreasing, yet the phase still holds the tetragonal crystal lattice (figure S4(b)). The crystal lattice gets increasingly distorted as the proton concentration increases and the structure becomes monoclinic at the end of the first-electron reaction at 1.05 V (figure 2(a) and figure 3). Kordesch et al. proposed that the first-electron reaction of MnO_2 in a Zn/MnO_2 alkaline battery is a solid-solution intercalation reaction.[28] This reaction is a homogeneous step because Mn-O bonding in the host MnO_2 is retained during proton intercalation. The theoretical voltage for the β-MnO_2 | γ-MnOOH redox couple averages 1.28 V upon proton intercalation, which is located within the experimental voltage curve of the first-electron reaction (figure 2(b)).

In addition the XRD results indicate Mn_3O_4 species at the end of first discharge (0.50 V) in figure 2(a). Mn_3O_4 has the tetrahedral crystal lattice where corner-sharing Mn-O tetrahedrons and edge-sharing Mn-O octahedrons are interconnected (figure 3). It is noted that Mn_3O_4 is unlikely to reduce from γ-MnOOH by electrochemical reaction because Mn_3O_4 has incorporating two Mn^{3+} and only one Mn^{2+}, which would indicate the involvement of only 1/3 electron. The first discharge is a two-electron reaction as its experimental capacity is 574 mAh g^{-1}, which is approximately 93% of theoretical capacity of MnO_2's two electrons. Therefore Mn^{2+} species should be formed at the end of the first discharge. It has been reported that MnOOH is reduced to $Mn(OH)_2$ by a two-phase conversion reaction (Eq. (2))[29-30] and Mn_3O_4 is formed by a parallel chemical reaction (Eq. (5))[12, 30] in the alkaline batteries. $Mn(OH)_2$ has the trigonal crystal lattice where the layer of edge-sharing M-O octahedrons and the layer of the proton are aligned along

the c-axis as shown in figure 3. Mn_3O_4 is generated by the chemical reaction between MnOOH and $Mn(OH)_2$ while the β-MnO_2 reduces to $Mn(OH)_2$ electrochemically. We estimate this chemical reaction proceeds further while collecting the XRD sample for a cathode by *ex situ* methods. Additional Mn_3O_4 begins to form after the electrochemical test stopped at the end of first discharge (0.50 V) and its amount increases extensively until the *ex situ* sample is collected. Donne et al. demonstrated that the formation of Mn_3O_4 is a kinetically limited reaction.[29] They measured Mn_3O_4 when experiments were tested over the extended time duration. Hertzberg et al., however, did not detect the Mn_3O_4 but $Mn(OH)_2$ while conducting *in situ* X-ray diffractometer.[13] Mn_3O_4 formation is alleviated in the relatively short-time frame between stopping the electrochemical reaction and measuring its XRD spectra. It is noted that the theoretical voltage of γ-MnOOH | $Mn(OH)_2$ redox couple demonstrates the formation of $Mn(OH)_2$ during the first discharge. The voltage is 0.93 V, which corresponds well with the experimental voltage plateau during the second-electron reaction (figure 2(b)).

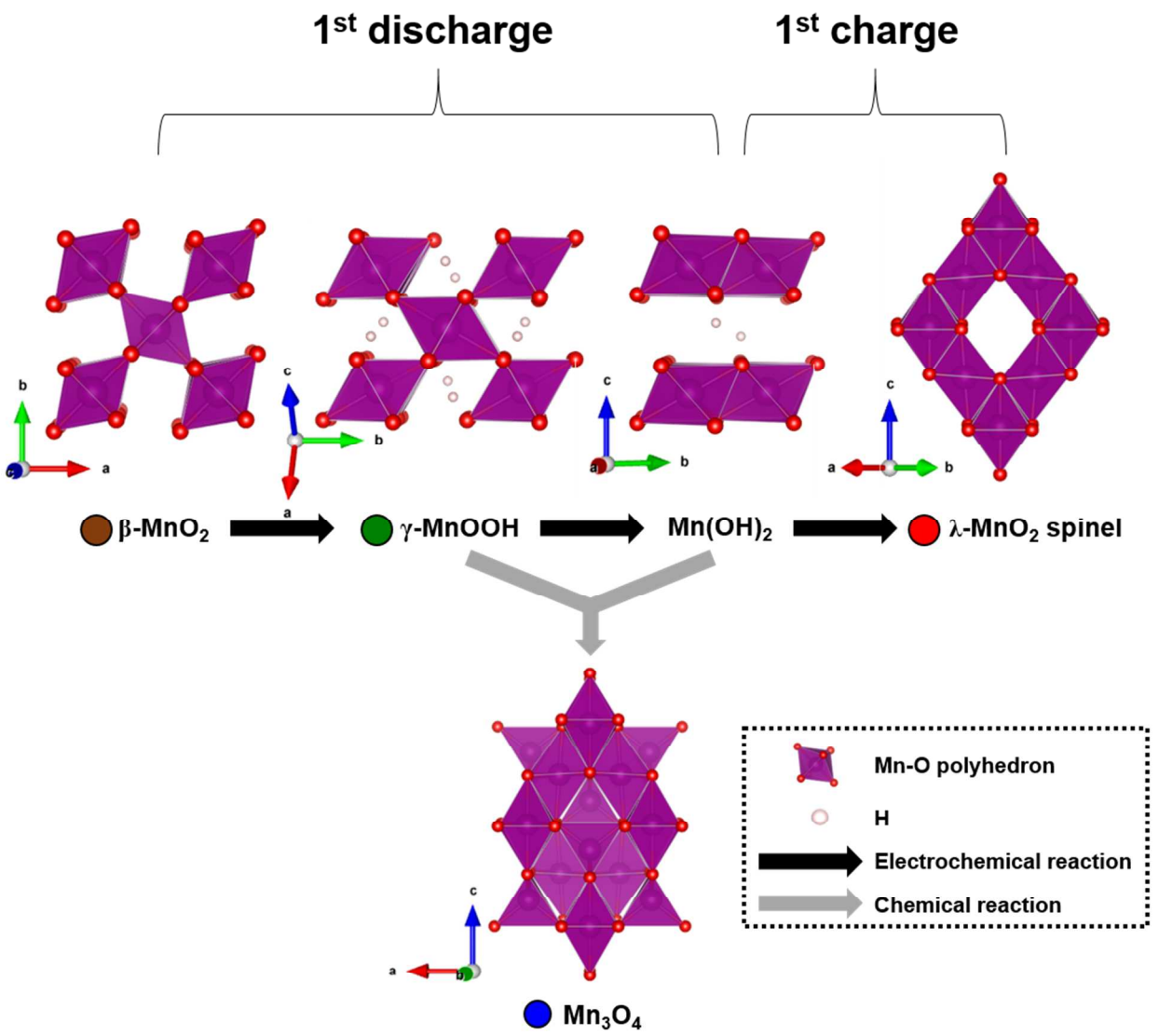

Figure 3. Schematic illustration of the electrochemical reaction mechanism of nanosized β-MnO_2 during the first cycle.

At the end of the first charge, λ-MnO_2 is measured (figure 2(a)) as a result of $Mn(OH)_2$ oxidation (Eq. (3)). λ-MnO_2 is a spinel phase with the cubic crystal lattice where M-O octahedrons are interconnected in an edge-sharing manner creating a 3D network of 1 x 1 void channel (figure 3). The XRD pattern of the cell at 1.80 V has a peak at ~19.1º, which corresponds to the (111) plane of λ-MnO_2 (figure S5(b)). This peak is the characteristic Bragg diffraction found in the λ-MnO_2

phase exclusively among the MnO_2 polymorphs (figure S5(a)). It is important to note that the XRD pattern at 1.80 V is weak and broadened. We attribute this phenomenon to the formation of nano-structured λ-MnO_2 particles, which are less than ~50 nm (figure S6). In very small particles, a large fraction of the atoms are located on the surface region, which undergo the structural relaxation for thermodynamic stability. Relaxed atoms are distorted from the original atomic positions of the crystal lattice, which could lead to the low intensity and peak broadening in the XRD pattern. Gallaway et al. reported that the irreversible $ZnMn_2O_4$ phase can be generated during the operation of primary alkaline batteries.[12] In our study, however, the XRD pattern at the first charged state does not indicate $ZnMn_2O_4$ phase (figure S4(e)). Also, no Zn 2p signal is found from XPS at the first charged state (figure S7(a)). We estimate that the formation of $ZnMn_2O_4$ is dependent on the rate of reaction. It is reported that $ZnMn_2O_4$ is not formed at fast C-rate, but generated at slow C-rate during the first discharge.[12]

Also, we investigated the formation of possible Ni hydroxide phases including β-NiOOH as a result of Ni oxidation (figure S8), however their XRD patterns were not aligned with the XRD pattern at the first charged state (1.80 V). Considering the λ-MnO_2, the theoretical voltage of $Mn(OH)_2$ | λ-MnO_2 redox couple (1.12 V) supports its formation, which is approximately the experimental voltage plateau during the first charge shown in figure 2(b). The first charge capacity is 353 mAh g^{-1}, which is 57 % of the theoretical capacity for the two-electron reaction. We ascribe the capacity loss to any unreacted $Mn(OH)_2$ which dissolves in the electrolyte as OH^- coordinated-complex ions or $[Mn(OH)_{n+2}]^{n-}$,[31] because Mn^{2+} in $Mn(OH)_2$ is soluble in highly concentrated basic solution. It is interesting that Mn_3O_4 which is generated during the first discharge is not measured at 1.80 V because it is also oxidized to λ-MnO_2 (Eq. (4)). Mn_3O_4 has poor electrical conductivity (10^8 ohm□cm) which hinders electrochemical reactions in Zn/MnO_2

alkaline batteries.[12] However, Mn_3O_4 converts into λ-MnO_2 in this study and we attribute it to the particle size of Mn_3O_4. We think that our synthesized active materials remain as nanoscale particles during phase transformations, which compensates for the intrinsic high resistivity of Mn_3O_4 and facilitates electrochemical reactions. Compared to bulky Mn_3O_4, nanoscale Mn_3O_4 has advantages in terms of large electrode/electrolyte interface for electrochemical reactions, superior conductivity through its ability to embed into carbon networks, and short electron/ion transport distance.[32] Recently, nano-sized Mn_3O_4 has been reported on for displaying high reversible capacity and enhanced CE as an anode material in Li-ion batteries.[32-34] The theoretical redox potential of Mn_3O_4 | λ-MnO_2 is calculated as 1.28 V, which is also close to the experimental voltage plateau observed during the charge (figure 2(b)).

The reaction mechanism at the hundredth cycle. The *ex situ* SXRD pattern is measured at the hundredth discharged/charged state of the synthesized β-MnO_2 cathode in the Zn/β-MnO_2 alkaline battery (figure 4(a,c)). It is interesting to note that the $ZnMn_2O_4$ phase is found, which was not formed during first cycle. This phase exists in both discharged/charged states because of its irreversibility in alkaline solutions. A Li and H co-inserted λ-MnO_2 spinel is also formed at the hundredth discharged state as shown in figure 4(a). The 111 and 311 peaks from the reference Li and H co-inserted λ-MnO_2 spinel align with the peaks from *ex situ* SXRD. The presence of Li is confirmed at the hundredth discharge state by XPS spectra with a signal in the Li 1s region shown in figure 4(b), which supports the formation of Li contained phase. We investigated other lithiated λ-MnO_2 spinel phases as the function of Li concentration to see if their XRD patterns match the *ex situ* SXRD pattern at the hundredth discharged state. However, there are no other phases that demonstrate as good a match as shown in figure S9. As the lithium

concentration in the λ-MnO_2 spinel increases, the peak positions of XRD shift to low diffraction angle (2θ) values. These values do not correspond to the *ex situ* SXRD pattern at the hundredth discharged state. It should be noted that the specific stoichiometry of the Li and H co-inserted λ-MnO_2 spinel is not defined quantitatively, however, we anticipate the Li and H co-inserted λ-MnO_2 spinel is generated based on our *ex situ* SXRD and XPS.

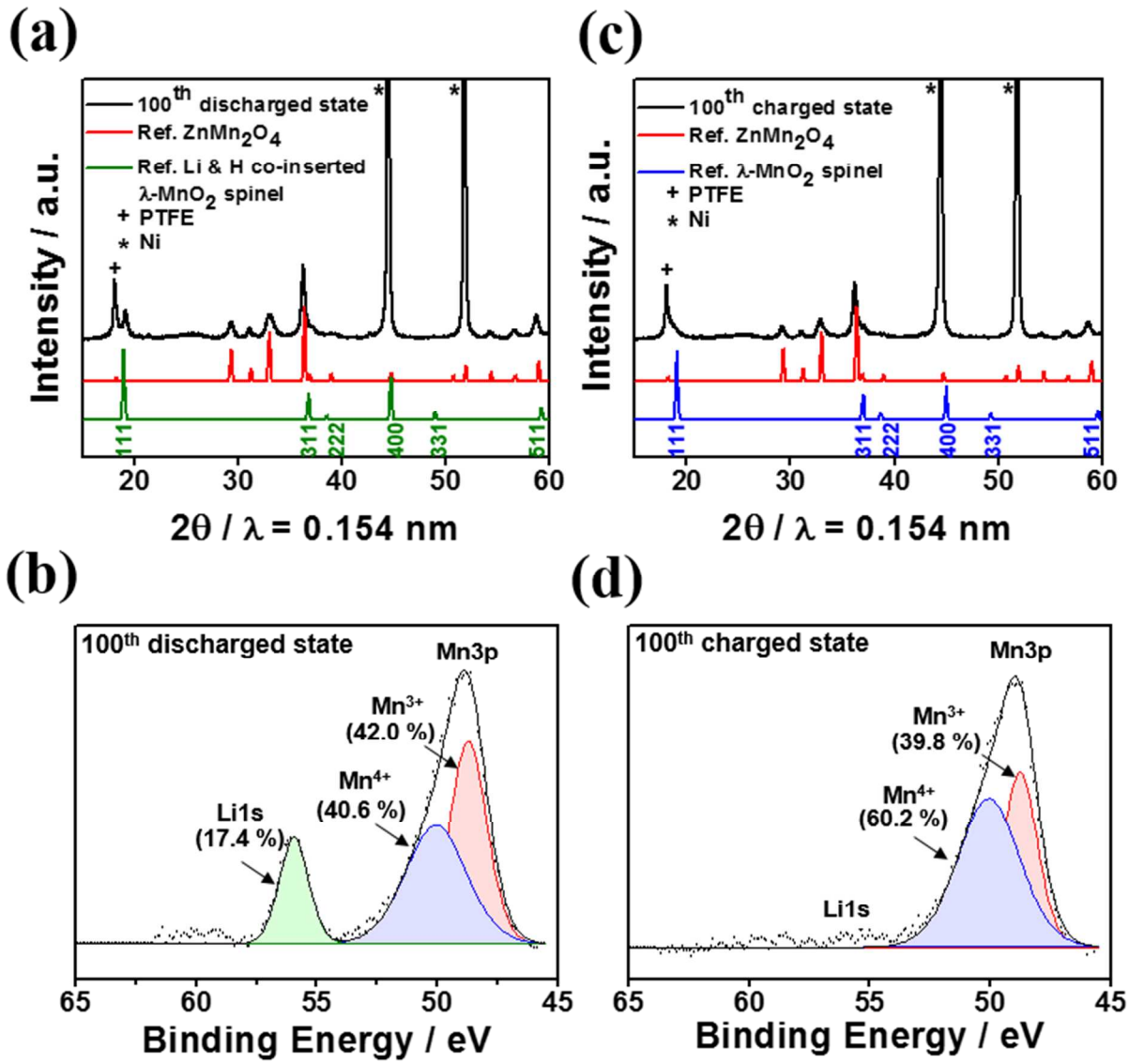

Figure 4. (a) *Ex situ* SXRD pattern from the cathode at the hundredth discharged state, the reference $ZnMn_2O_4$ (ICSD #15305) and the reference Li & H co-inserted λ-MnO_2 spinel (ICSD #85606); (b) XPS spectra for Li 1s and Mn 3p region from the cathode at the hundredth discharged state; (c) *Ex situ* SXRD pattern from the cathode at the hundredth charged state, the reference $ZnMn_2O_4$ (ICSD #15305) and the reference λ-MnO_2 spinel (ICSD #193445); (d) XPS spectra for Li 1s and Mn 3p region from the cathode at the hundredth charged state.

We estimate delithiated λ-MnO_2 spinel is formed at the hundredth charged state as shown in figure 4(c). It is noted that the right side of asymmetrically broadened peak at ~19.1º in the SXRD pattern matches the (111) peak in the reference XRD pattern of λ-MnO_2 (figure S10). This asymmetric peak belongs to the convoluted peak from PTFE and λ-MnO_2. We believe this phase is formed by the extraction of Li and H process during charging as shown in figure 5. There is no detection of Li in the Li 1s region from the XPS spectrum, which is evidence for the formation of the delithiated spinel phase. In addition, the XPS spectrum for surface Mn species can be used for qualitative understanding of elements' change. The increase in the ratio of Mn^{4+} species to Mn^{3+} species indicates delithiation upon charging as shown in figure 4(b, d). Assignments for Mn 3p of ~50 eV (Mn^{4+}) and ~48.5 eV (Mn^{3+}) were made based on the previous reports.[35-36] The ratio is approximately 1:1 at the hundredth discharge which increases to 3:2 at the hundredth charge. Mn^{3+} is partially oxidized to Mn^{4+} when Li^+ and H^+ leave the cathode. We demonstrate the voltage curve at the hundredth cycle combining with the voltage curve at the first cycle for comparison in figure S11.

We measure irreversible $ZnMn_2O_4$ from both the hundredth discharge/charge states in the *ex situ* SXRD pattern (figure 4(a, c)). In Zn/MnO_2 alkaline batteries, $Zn(OH)_4^{2-}$ is formed during the discharge reaction:[26]

$$Zn + 4OH^- \rightarrow Zn(OH)_4^{2-} + 2e^- \quad (7)$$

Once $Zn(OH)_4^{2-}$ is formed, it chemically reacts with MnOOH at the cathode:[37]

$$2MnOOH + Zn(OH)_4^{2-} \rightarrow ZnMn_2O_4 + 2H_2O + 2OH^- \quad (8)$$

$ZnMn_2O_4$ has a tetrahedral crystal lattice where corner-sharing Zn-O tetrahedrons and edge-sharing Mn-O octahedrons are interconnected (figure 5). Mn and Zn have 3+ and 2+ oxidation

states, respectively. $ZnMn_2O_4$ is known to have higher resistivity than MnO_2 by six orders of magnitude, which causes a loss of conductivity in the cathode.[12] In this study, $ZnMn_2O_4$ is not found after the first cycle as shown in figure 2(a), however, it is seen in the hundredth cycle in both the discharged/charged states as shown in figure 4. The amount of $ZnMn_2O_4$ in the cathode increases as the cycle of Zn/β-MnO_2 alkaline battery proceeds, which leads to capacity fading.

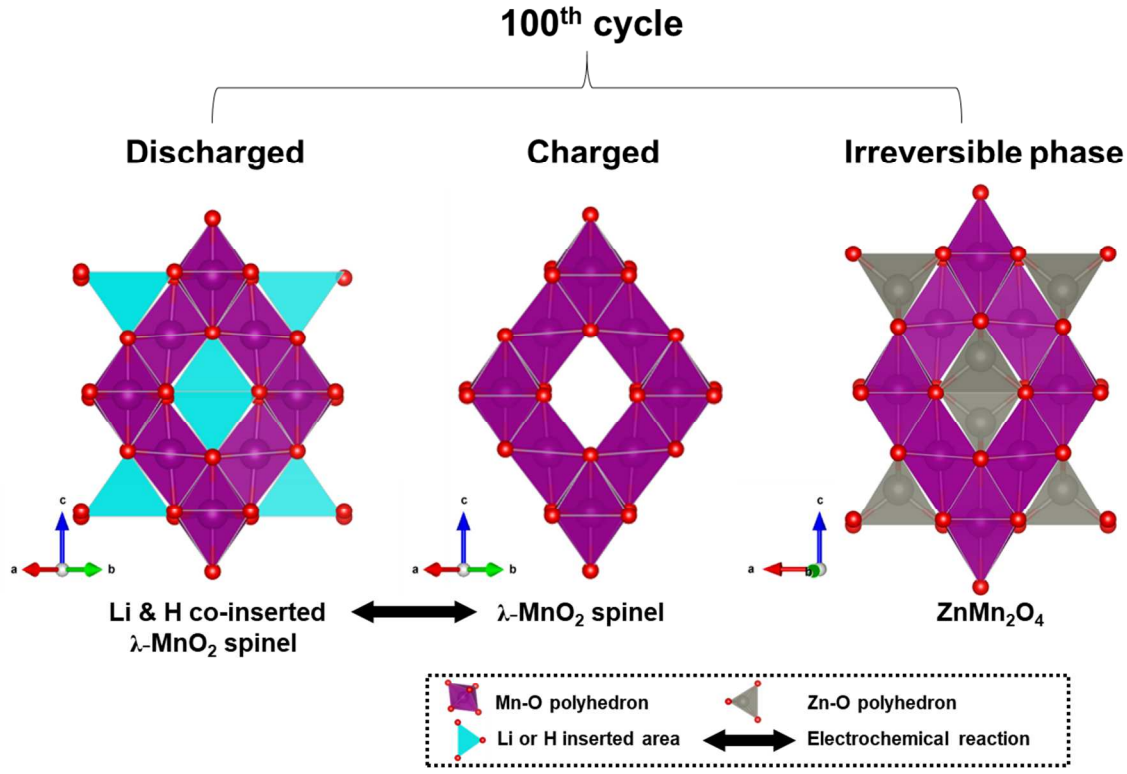

Figure 5. The reaction mechanism of β-MnO_2 during the hundredth cycle.

The effect of Bi_2O_3 additive. It has been reported that the addition of Bi^{3+} either chemically or physically to the MnO_2 cathode improves the cycling performance of Zn-based aqueous batteries.[38-41] Dzieciuch et al. reported that Bi_2O_3 in the MnO_2 cathode of alkaline batteries using KOH electrolytes inhibits $ZnMn_2O_4$ formation to some level.[40] In another study, Shin et al. found

that the zincate ion is deposited on Bi_2O_3 and prolongs the cycle life of Zn-based batteries.[41] In order to study the effect of the Bi^{3+} compound on nanosized β-MnO_2 in the 1 M KOH and 3 M LiOH electrolyte, we physically mix Bi_2O_3 into the synthesized β-MnO_2 nanomaterial with 4% mole fraction and measure the performance of Zn/β-MnO_2 alkaline battery. The discharge capacity measured is 316 mAh g^{-1} at the hundredth cycle (figure 6(a)). This indicates increased capacity compared to the commercial β-MnO_2 and synthesized β-MnO_2 nanomaterial (112 and 225 mAh g^{-1}, respectively). The CE is less than 100 % due to the H_2 and O_2 gas evolution within the operating voltage window of a battery as was discussed earlier. Furthermore, the synthesized β-MnO_2 nanomaterial with Bi_2O_3 incorporated demonstrates improved specific capacity over a range of rates as shown in figure 6(b). This exhibits higher discharge capacity and better cycling stability than the synthesized β-MnO_2 without Bi_2O_3. To be specific, the synthesized β-MnO_2 with Bi_2O_3 has an average capacity of 506 mAh g^{-1} during the first stage and retains 86% of that initial capacity (434 mAh g^{-1}) at the last stage. Comparatively, the synthesized β-MnO_2 without Bi_2O_3 has an average capacity of 403 mAh g^{-1} at the first stage and 292 mAh g^{-1} at the last stage, indicating 72% recovery. In order to investigate the role of Bi_2O_3 in the rechargeable Zn/MnO_2 alkaline chemistry, Bi_2O_3 powder was immersed in the 6 M Zn nitrate solution. SEM images show that original disordered structures transform to relatively ordered structures with island meshes in a Zn^{2+} solution (figure S12). The EDS mapping for immersed Bi_2O_3 powder that was carefully cleansed and dried indicates the presence of Zn species on the surface of the Bi_2O_3 (figure S13). These SEM and EDS analyses imply that Zn^{2+} reacts with the surface Bi_2O_3. In addition, we took EDS of synthesized β-MnO_2 with and without Bi_2O_3 at the hundredth charged state as shown in figure S14. We find that the atomic percent of Zn out of Mn and Zn reduces from 11.71 % to 8.84 % in the synthesized β-MnO_2 with Bi_2O_3, indicating Bi_2O_3 additive

alleviates the formation of $ZnMn_2O_4$. As was discussed for Zn/MnO_2 alkaline batteries, $Zn(OH)_4^{2-}$ or potentially a combination of Zn^{2+} and OH^- in alkaline solution undergo chemical reactions with Mn species to produce an electrochemically irreversible phase consisting of $ZnMn_2O_4$. Our results suggest that the formation of $ZnMn_2O_4$ can be alleviated through $Zn(OH)_4^{2-}$ reactions with Bi_2O_3 which lessens the likelihood that Mn species will react with $Zn(OH)_4^{2-}$.

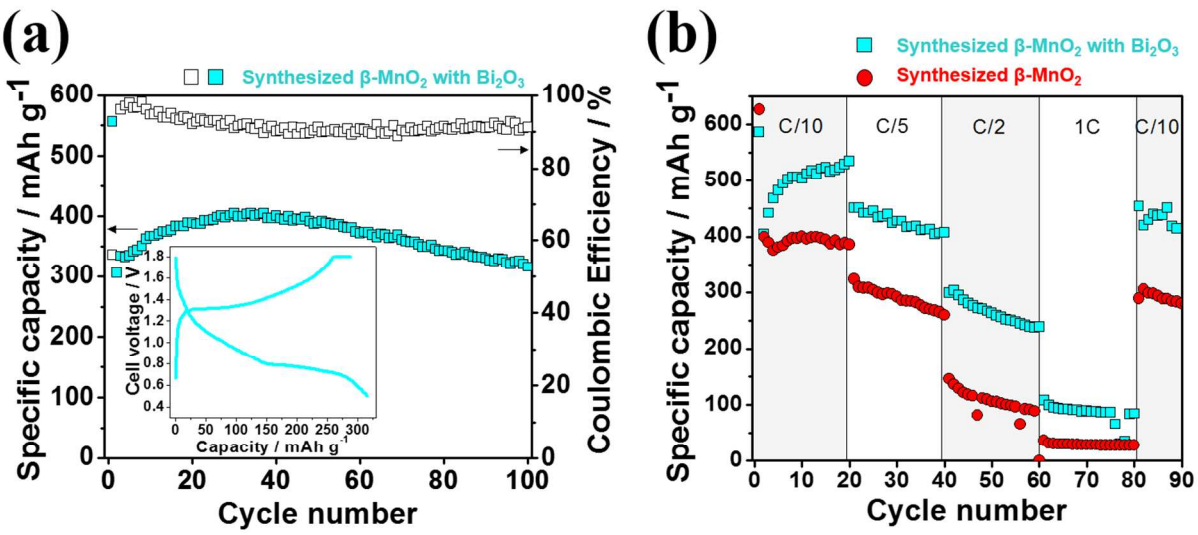

Figure 6. (a) Cyclic performance for the synthesized β-MnO_2 with Bi_2O_3 additive. The inset indicates the voltage curve at the hundredth cycle; (b) Rate capability test for the synthesized β-MnO_2 with and without the Bi_2O_3 additive are conducted with C/10, C/5, C/2, 1C, and C/10 in sequence.

CONCLUSIONS

This study has demonstrated that synthesized β-MnO_2 nanomaterials have high utility for rechargeable $Zn/$β-MnO_2 alkaline batteries. The nanosized β-MnO_2 cathode in the 1 M KOH and

3 M LiOH mixed electrolyte shows higher rechargeable capacity compared to the bulky β-MnO_2 cathode's capacity. The β-MnO_2 nanomaterials have large surface area and strong surface-chemisorption property to facilitate electrochemical reactions in alkaline solutions. In addition, the phase transformation of synthesized β-MnO_2 nanomaterial involves proton intercalation reactions followed by two-phase conversion reactions during the first cycle. At the hundredth cycle, Li and H intercalate together into the host structure of λ-MnO_2 spinel. Additionally the physical incorporation of Bi_2O_3 into synthesized β-MnO_2 nanomaterials shows an excellent discharge capacity of 316 mAh g^{-1} at the hundredth cycle. The findings of this study may provide useful insights towards the development of rechargeable Zn/MnO_2 alkaline batteries in high-energy and low-cost stationary energy storage.

ASSOCIATED CONTENT

Supporting Information

Standard reduction potentials, standard Gibbs free energy of formation, Mn 3s splitting in the XPS result of commercial β-MnO_2, Nitrogen adsorption/desorption isotherm of the β-MnO_2 and BET surface areas, the electrochemical stability window of 1M KOH and 3M LiOH electrolytes on Ni foam electrodes, in-house XRD patterns for synthesized β-MnO_2 nanomaterial and its intermediates during the first cycle, XRD patterns of MnO_2 polymorphs from the ICSD database, and in-house XRD pattern for synthesized β-MnO_2 nanomaterial at the first charged state (1.80 V), the SEM image of MnO_2 cathode at the first charged state (1.80 V), the XPS spectra for Zn 2p region from the cathode at the first and the hundredth charged state, the XRD pattern measured at the first charged state (1.80 V) and possible Ni hydroxides phases, XRD patterns of

lithiated Mn oxide spinels from ICSD database and the SXRD pattern at the hundredth discharge, the SXRD pattern measured at the hundredth charged state, the comparison of voltage curves between the first and the hundredth cycle, SEM images of Bi_2O_3 and immersed Bi_2O_3 in 6M Zn nitrate solution with corresponding EDS mapping for Zn $K\alpha_1$ and Bi $M\alpha_1$, and SEM images and the corresponding EDS of the hundredth charged state for MnO_2 cathode with and without Bi_2O_3 (PDF)

AUTHOR INFORMATION

Corresponding Author

*E-mail: shmeng@ucsd.edu.

Present Addresses

§(J.S.) Advanced Battery Center, KAIST Institute for NanoCentury, Korea Advanced Institute of Science and Technology (KAIST), 291 Daehak-ro, Yuseong-gu, Daejeon, 34141, Republic of Korea.

Notes

The authors declare no competing financial interest.

ACKNOWLEDGMENTS

Joon Kyo Seo is grateful for William Getz and Fei Ji for fruitful discussions. This research was funded by the Advanced Research Projects Agency - Energy (ARPA-E), U.S. Department of

Energy (award number DE-AR0000535). The authors wish to acknowledge the computation facilities at the Extreme Science and Engineering Discovery Environment (XSEDE), which is supported by National Science Foundation (No. ACI-1053575). The SEM analysis in this work was performed at the San Diego Nanotechnology Infrastructure (SDNI), a member of the National Nanotechnology Coordinated Infrastructure, which is supported by the National Science Foundation (No. ECCS-1542148). We performed XPS experiments at the University of California, Irvine Materials Research Institute (IMRI) using instrumentation funded in part by the National Science Foundation Major Research Instrumentation Program (grant number CHE-1338173). The authors extend their gratitude for the precious beam time and assistance from scientists at beamlines 11-BM in Argonne National Laboratory. The separator (FS 22145) was provided from Freudenberg LLC.

REFERENCES

(1) Gallaway, J. W.; Erdonmez, C. K.; Zhong, Z.; Croft, M.; Sviridov, L. A.; Sholklapper, T. Z.; Turney, D. E.; Banerjee, S.; Steingart, D. A. Real-Time Materials Evolution Visualized within Intact Cycling Alkaline Batteries. *J. Mater. Chem. A* **2014**, *2*, 2757-2764.

(2) Ingale, N. D.; Gallaway, J. W.; Nyce, M.; Couzis, A.; Banerjee, S. Rechargeability and Economic Aspects of Alkaline Zinc–Manganese Dioxide Cells for Electrical Storage and Load Leveling. *J. Power Sources* **2015**, *276*, 7-18.

(3) Turney, D. E., et al. Rechargeable Zinc Alkaline Anodes for Long-Cycle Energy Storage. *Chem. Mater.* **2017**, *29*, 4819-4832.

(4) Julien, C. M.; Massot, M.; Poinsignon, C. Lattice Vibrations of Manganese Oxides: Part I. Periodic Structures. *Spectrochimica Acta Part A: Molecular and Biomolecular Spectroscopy* **2004**, *60*, 689-700.

(5) Zhang, K.; Han, X.; Hu, Z.; Zhang, X.; Tao, Z.; Chen, J. Nanostructured Mn-Based Oxides for Electrochemical Energy Storage and Conversion. *Chem. Soc. Rev.* **2015**, *44*, 699-728.

(6) Patrice, R.; Gérand, B.; Leriche, J. B.; Seguin, L.; Wang, E.; Moses, R.; Brandt, K.; Tarascon, J. M. Understanding the Second Electron Discharge Plateau in Mno2-Based Alkaline Cells. *J. Electrochem. Soc.* **2001**, *148*, A448-A455.

(7) McBreen, J. The Electrochemistry of B-Mno2 and Γ-Mno2 in Alkaline Electrolyte. *Electrochim. Acta* **1975**, *20*, 221-225.

(8) Boden, D.; Venuto, C. J.; Wisler, D.; Wylie, R. B. The Alkaline Manganese Dioxide Electrode: I . The Discharge Process. *J. Electrochem. Soc.* **1967**, *114*, 415-417.

(9) Lee, B.; Yoon, C. S.; Lee, H. R.; Chung, K. Y.; Cho, B. W.; Oh, S. H. Electrochemically-Induced Reversible Transition from the Tunneled to Layered Polymorphs of Manganese Dioxide. *Sci. Rep.* **2014**, *4*, 6066.

(10) Lee, B.; Seo, H. R.; Lee, H. R.; Yoon, C. S.; Kim, J. H.; Chung, K. Y.; Cho, B. W.; Oh, S. H. Critical Role of Ph Evolution of Electrolyte in the Reaction Mechanism for Rechargeable Zinc Batteries. *ChemSusChem* **2016**, *9*, 2948-2956.

(11) Pan, H., et al. Reversible Aqueous Zinc/Manganese Oxide Energy Storage from Conversion Reactions. *Nat. Energy* **2016**, *1*, 16039.

(12) Gallaway, J. W.; Menard, M.; Hertzberg, B.; Zhong, Z.; Croft, M.; Sviridov, L. A.; Turney, D. E.; Banerjee, S.; Steingart, D. A.; Erdonmez, C. K. Hetaerolite Profiles in Alkaline Batteries Measured by High Energy Edxrd. *J. Electrochem. Soc.* **2015**, *162*, A162-A168.

(13) Hertzberg, B. J., et al. Effect of Multiple Cation Electrolyte Mixtures on Rechargeable Zn–Mno2 Alkaline Battery. *Chem. Mater.* **2016**, *28*, 4536-4545.

(14) Chen, J.; Cheng, F. Combination of Lightweight Elements and Nanostructured Materials for Batteries. *Acc. Chem. Res.* **2009**, *42*, 713-723.

(15) Cheng, F.; Zhao, J.; Song, W.; Li, C.; Ma, H.; Chen, J.; Shen, P. Facile Controlled Synthesis of Mno2 Nanostructures of Novel Shapes and Their Application in Batteries. *Inorg. Chem.* **2006**, *45*, 2038-2044.

(16) Kresse, G.; Furthmüller, J. Efficient Iterative Schemes for Ab Initio Total-Energy Calculations Using a Plane-Wave Basis Set. *Phys. Rev. B* **1996**, *54*, 11169-11186.

(17) Dudarev, S. L.; Botton, G. A.; Savrasov, S. Y.; Humphreys, C. J.; Sutton, A. P. Electron-Energy-Loss Spectra and the Structural Stability of Nickel Oxide:An Lsda+U Study. *Phys. Rev. B* **1998**, *57*, 1505-1509.

(18) Perdew, J. P.; Burke, K.; Ernzerhof, M. Generalized Gradient Approximation Made Simple. *Phys. Rev. Lett.* **1996**, *77*, 3865-3868.

(19) Blöchl, P. E. Projector Augmented-Wave Method. *Phys. Rev. B* **1994**, *50*, 17953-17979.

(20) Kresse, G.; Joubert, D. From Ultrasoft Pseudopotentials to the Projector Augmented-Wave Method. *Phys. Rev. B* **1999**, *59*, 1758-1775.

(21) Kresse, G.; Furthmüller, J. Efficiency of Ab-Initio Total Energy Calculations for Metals and Semiconductors Using a Plane-Wave Basis Set. *Comput. Mater. Sci.* **1996**, *6*, 15-50.

(22) Persson, K. A.; Waldwick, B.; Lazic, P.; Ceder, G. Prediction of Solid-Aqueous Equilibria: Scheme to Combine First-Principles Calculations of Solids with Experimental Aqueous States. *Phys. Rev. B* **2012**, *85*, 235438.

(23) Stranick, M. A. Mno2 by Xps. *Surf. Sci. Spectra* **1999**, *6*, 31-38.

(24) Han, B. C.; Miranda, C. R.; Ceder, G. Effect of Particle Size and Surface Structure on Adsorption of O and Oh on Platinum Nanoparticles: A First-Principles Study. *Phys. Rev. B* **2008**, *77*, 075410.

(25) Seo, J. K.; Khetan, A.; Seo, M. H.; Kim, H.; Han, B. First-Principles Thermodynamic Study of the Electrochemical Stability of Pt Nanoparticles in Fuel Cell Applications. *J. Power Sources* **2013**, *238*, 137-143.

(26) Dirkse, T. P. The Behavior of the Zinc Electrode in Alkaline Solutions: Iii . The Equilibrium Potential. *J. Electrochem. Soc.* **1979**, *126*, 1456-1459.

(27) Bratsch, S. G. Standard Electrode Potentials and Temperature Coefficients in Water at 298.15 K. *J. Phys. Chem. Ref. Data* **1989**, *18*, 1-21.

(28) Kordesch, K.; Gsellmann, J.; Tomantschger, K. The Alkaline Manganese Dioxide-Zinc Cell. *J. Electroanal. Chem. Interfacial Electrochem.* **1981**, *118*, 187-201.

(29) Donne, S. W.; Lawrance, G. A.; Swinkels, D. A. J. Redox Processes at the Manganese Dioxide Electrode: Ii. Slow-Scan Cyclic Voltammetry. *J. Electrochem. Soc.* **1997**, *144*, 2954-2961.

(30) Binder, L.; Kordesch, K.; Urdl, P. Improvements of the Rechargeable Alkaline Mno2 □ Zn Cell. *J. Electrochem. Soc.* **1996**, *143*, 13-17.

(31) Kozawa, A.; Kalnoki-Kis, T.; Yeager, J. F. Solubilities of Mn(Ii) and Mn(Iii) Ions in Concentrated Alkaline Solutions. *J. Electrochem. Soc.* **1966**, *113*, 405-409.

(32) Wang, J.-G.; Jin, D.; Zhou, R.; Li, X.; Liu, X.-r.; Shen, C.; Xie, K.; Li, B.; Kang, F.; Wei, B. Highly Flexible Graphene/Mn3o4 Nanocomposite Membrane as Advanced Anodes for Li-Ion Batteries. *ACS Nano* **2016**, *10*, 6227-6234.

(33) Gao, J.; Lowe, M. A.; Abruña, H. D. Spongelike Nanosized Mn3o4 as a High-Capacity Anode Material for Rechargeable Lithium Batteries. *Chem. Mater.* **2011**, *23*, 3223-3227.

(34) Wang, H.; Cui, L.-F.; Yang, Y.; Sanchez Casalongue, H.; Robinson, J. T.; Liang, Y.; Cui, Y.; Dai, H. Mn3o4−Graphene Hybrid as a High-Capacity Anode Material for Lithium Ion Batteries. *J. Am. Chem. Soc.* **2010**, *132*, 13978-13980.

(35) McCloy, J. S.; Leslie, C.; Kaspar, T.; Jiang, W.; Bordia, R. K. Magnetic Behavior of Ni and Co Doped Cumn2o4 Spinels. *Journal of Applied Physics* **2012**, *111*, 07E149.

(36) Töpfer, J.; Feltz, A.; Gräf, D.; Hackl, B.; Raupach, L.; Weissbrodt, P. Cation Valencies and Distribution in the Spinels Nimn2o4 and Mznimn2−Zo4 (M = Li, Cu) Studied by Xps. *physica status solidi (a)* **1992**, *134*, 405-415.

(37) Sharma, Y.; Haynes, A.; Binder, L.; Kordesch, K. The Effect of the Amount of Electrolyte in the Anode Gel on the Rechargeability of Alkaline Manganese Dioxide ・ Zinc Cells. *J. Power Sources* **1989**, *27*, 145-153.

(38) Yao, Y. F.; Gupta, N.; Wroblowa, H. S. Rechargeable Manganese Oxide Electrodes. *J. Electroanal. Chem. Interfacial Electrochem.* **1987**, *223*, 107-117.

(39) Wroblowa, H. S.; Gupta, N. Rechargeable Manganese Oxide Electrodes. *J. Electroanal. Chem. Interfacial Electrochem.* **1987**, *238*, 93-102.

(40) Dzieciuch, M. A.; Gupta, N.; Wroblowa, H. S. Rechargeable Cells with Modified Mno2 Cathodes. *J. Electrochem. Soc.* **1988**, *135*, 2415-2418.

(41) Shin, J.; You, J.-M.; Lee, J. Z.; Kumar, R.; Yin, L.; Wang, J.; Meng, Y. S. Deposition of Zno on Bismuth Species Towards Rechargeable Zn-Based Aqueous Battery. *Phys. Chem. Chem. Phys.* **2016**, *18*, 26376.

TABLE OF CONTENTS